Sensors and Actuators B 206 (2015) 212–219

Contents lists available at ScienceDirect

Sensors and Actuators B: Chemical

journal homepage: www.elsevier.com/locate/snb

Novel and high-performance LSPR biochemical fiber sensor

Yue-Jing He*

Department of Electronic Engineering, National Chin-Yi University of Technology, Taichung 41170, Taiwan, ROC

ARTICLE INFO

Article history:
Received 13 June 2014
Received in revised form
15 September 2014
Accepted 16 September 2014
Available online 28 September 2014

Keywords:
Optical chemical LSPR fiber sensors
Optical biological LSPR fiber sensors
Finite element method
Eigenmode expansion method
Perfectly matched layer
Perfectly reflecting boundary condition

ABSTRACT

To enhance further the performance of the current localized surface plasmon resonance (LSPR) biochemical fiber sensor, a novel design model for a short length, high resolution, and high sensitivity was developed in this study. Based on a cross-sectional view of the component, the proposed new LSPR biochemical fiber sensor comprises a single-mode fiber and two types of nano-metal gears. The difference between these two types of nano-metal gears is the angular displacement of a single pitch. In a cylindrical coordinate system, if the φ axis is considered a straight, the LSPR fiber sensor exhibits a clear tessellation array. The numerical simulation method that combines the finite element method (FEM) and eigenmode expansion method (EEM) was used to design and analyze the sensor. In addition, to increase the accuracy of the numerical simulation results, the proposed numerical simulation method included a perfectly matched layer (PML) and a perfectly reflecting boundary condition (PRB). After the design procedures had been performed, the LSPR biochemical fiber sensor designed in this study possesses the advantageous attributes of a short length (74.34779 μm), high resolution (−110 dB), and high sensitivity (93 987 nm/RIU). As far as I know, up to present it possesses the best resolution and sensitivity compared with the other LSPR sensors.

1. Introduction

The surface plasmon resonance (SPR) phenomenon sensed using optical fibers can be divided into two categories, namely, propagating SPR and localized surface plasmon resonance (LSPR). Propagating SPR can be obtained by coating a thin layer of metal onto the surface of an optical fiber. Surface plasmons occur when extended charge waves traveling on the interface between metal and glass are excited by a dispersion of output light that matches the incident light. Thus, surface plasmons are defined as evanescent electromagnetic waves bounded by metal–glass interfaces and induced by oscillations of the conduction electrons in metal. In recent years, several SPR sensors that feature a fiber optic structure have attracted the attention of scientists and engineers. These sensors provide highly sensitive and label-free biosensing for investigating the affinity between biological molecules, and are widely employed in the fields of biology, biochemistry, and genetic engineering [1–16]. LSPR refers to collective electron charge oscillations confined in metallic nanostructures, which exhibit enhanced near-field amplitude at the resonance wavelength. These unique optical properties are widely exploited for various applications including chemical and biological sensing, subwavelength optical waveguides, and surface-enhanced Raman scattering [17–33].

The sensitivity of LSPR depends on the size and geometry of nanostructures. In addition, at THZ or GHZ frequencies, the refractive index of metals is no longer related to frequency and is considered a constant. (Thus, metals are considered ideal electric conductors.) This condition is known as spoof SPR. In addition, electromagnetic waves, excluding those of radiation or diffraction, only occur on metal surfaces in certain forms [34–40].

According to the optic properties of the LSPR, they indicated that electrons collectively oscillated on the junctions between metal and analyte. It was the critical factor enabling the LSPR fiber sensors to be highly sensitive to analyte concentration variations. Consequently, for this novel LSPR biochemical fiber sensor, as the number of positions (or particles) where collective electrons oscillation can occur increases, the sensitivity of this sensor in measuring analyte concentrations increases. This research had two main objectives: (a) to design a high-performance LSPR biochemical fiber sensor based on nano-metal cylinder-tessellation array. Nonpropagation LSPR sensors are highly sensitive toward their geometric structure parameters and variations in analyte concentration. Therefore, numerical calculations have to be performed to acquire accurate design parameters before practically producing this sensor. In addition, two new techniques, namely the perfectly matched layer (PML) and perfectly reflecting boundary condition (PRB) [18], were incorporated into the previously proposed finite element method (FEM) and eigenmode expansion method (EEM) [17–19], thereby enhancing the precision of numerical simulation and providing effective design parameters for sensor production;

* Tel.: +886 423924505; fax: +886 423926610.
E-mail address: yuejing@ncut.edu.tw

http://dx.doi.org/10.1016/j.snb.2014.09.061
0925-4005/

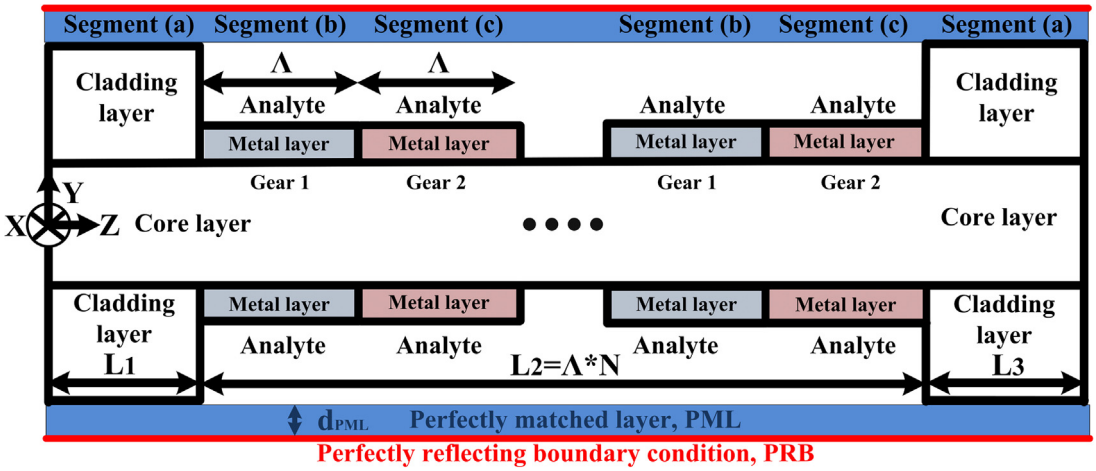

Fig. 1. The side structure diagram of novel LSPR biochemical fiber sensor.

(b) to compare this novel LSPR biochemical sensor with the current two kinds of LSPR sensors possessing a short length, high resolution, and high sensitivity.

The remainder of this paper is organized as follows: Section 2 provides a detailed description of this novel LSPR biochemical fiber sensor, including the geometric model, structural parameters, and material properties. Furthermore, the primary functions regarding the PML and PRB were briefly interpreted [17–19].

Section 3 provides a brief description of theories related to the FEM. Using the FEM that combines a PML and PRB, the various modes, including discrete guided modes, discrete LSPR modes, and discrete radiation modes, in Segments (a)–(c) (as shown in Figs. 1 and 2) can be obtained. The 2D power distribution of the core mode (HE_{11}) and radiation mode in Segment (a) were plotted to enable readers to understand the power distribution of the optic source and the definition of a discrete radiation mode. After the novel LSPR biochemical fiber sensor was designed, HE_{11} was input into the left end of the sensor (input port) to demonstrate the physical power transmission phenomenon in this novel sensor. Then, the 2D power distribution of LSPR waves and radiation modes in Segments (b) and (c) was also plotted to confirm that the current metallic patterns of fiber sensors can trigger LSPR wave through the electric fields E_r and E_φ of HE_{11}. The critical reason for the high performance of the novel fiber sensor is the generation of LSPR wave. From the perspective of numerical methods, the decomposition resolution of triangular elements influences the accuracy of the acquired modes. From a mathematical perspective, if all obtained modes are accurate, the orthogonal values between the modes must be 0. Thus, reverse thinking was employed to determine the allowable orthogonal value, that is, 10^{-4} ($10\cdot\log_{10}(10^{-4}) = -40$ dB), before the cutting resolutions were adjusted for simulation. In addition, for all modes of Segments (a)–(c) calculated in this section, separate orthogonal values were established to ensure that the modes satisfied the −40 dB criterion [17–19].

Section 4 briefly introduces theories related to the EEM. An explanation of how the EEM enables the modes to conduct propagations in the novel LSPR biochemical fiber sensor is provided. However, this numerical technique also encounters precision problems. Fourier series expansion is the critical principle that facilitates optical wave propagation when utilizing the EEM. In other words, if the number of modes is insufficient during the propagation process, even in non-absorbent media, the total power declines with increases in the number of Fourier series expansion implementations [1,17–19]. This study adopted the reverse-thinking concept and performed propagations using various numbers of guided modes to assess the power losses and determine the suitable number of guided modes for this research. Because of the absorbent material (gold) used in the sensor adopted for this study, when designing and analyzing the proposed LSPR biochemical fiber sensor, the power losses of all Fourier series expansion positions were assessed according to the original definition of power loss. The examination mechanism in [18] was adopted to inspect whether the power losses of all Fourier series expansion positions satisfied the −40 dB criterion.

In Section 5, the content of Sections 3 and 4 is summarized and a rigorous and simple procedure for analyzing and designing the novel LSPR biochemical fiber sensor is proposed. In addition, the simulation results are presented using numerous graphics. The performance of the LSPR biochemical fiber sensor designed in this paper was compared with two structures in [17,18].

In the final section, the numerical simulation method employed in this study is summarized, and the data obtained in Section 5 is used to confirm that the proposed novel LSPR biochemical fiber sensor possesses the excellent attributes of a short length (74.34779 μm), high resolution (approximately −110 dB), and high sensitivity (approximately 93 987 nm/RIU).

2. Novel LSPR biochemical fiber sensor

This study proposes a novel LSPR biochemical fiber sensor that comprises three structures, namely, a single-mode fiber (SMF) and two types of nano-metal gears. Figs. 1 and 2 show side and cross-sectional diagrams of the sensor structure. Segment (a) represents a general SMF. Segments (b) and (c) demonstrate the results of etching the entire cladding layer of Segment (a) and plating a metal material of dm thickness onto the core layer to create a gear-shaped geometric structure (containing 80 pins, $N_m = 80$). The difference between the two types of nano-metal gears is the angular displacement of a single pitch. In a cylindrical coordinate system, if the φ axis is considered a straight, the LSPR biochemical fiber sensor exhibits a clear tessellation array. To avoid misunderstandings for Figs. 1 and 2 in Ref. [18], Figs. 1 and 2 in this study have been modified by using Gear 1 and Gear 2. The structural parameters of the sensor were set as follows: $a_1 = 2.25$ μm, $a_2 = 5.25$ μm, $d_m = 0.02$ μm, $d_{PML} = 0.825$ μm, $n_1 = 1.454$, $n_2 = 1.43$, $n_m = 0.56246309 + j9.840798407$ ($\lambda = 1550$ nm), $n_a = 1.33$ (the refractive index of analyte), $\Lambda = 181.1593$ nm, $N = 300$, $N_m = 80$, duty cycle = 0.5, $L_1 = 10$ μm, $L_2 = N \times \Lambda = 54.34779$ μm, and $L_3 = 10$ μm. The length of the LSPR biochemical fiber sensor was $L = L_1 + L_2 + L_3 = 74.34779$ μm.

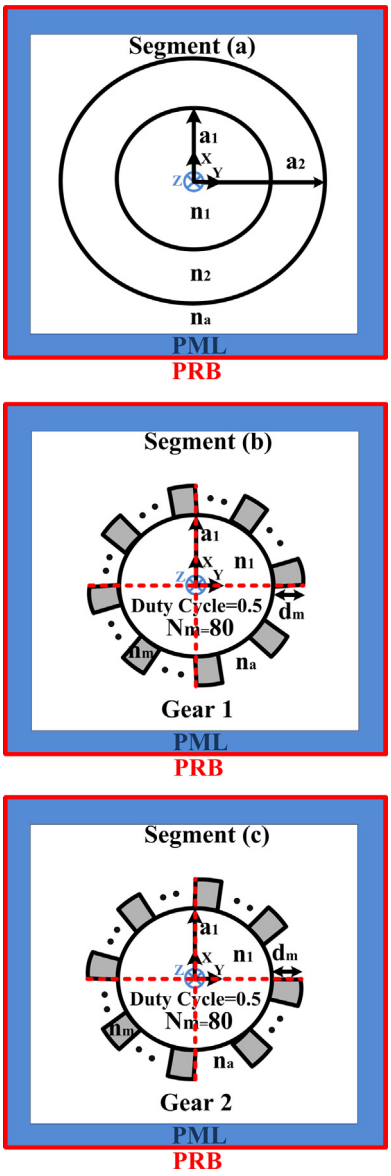

Fig. 2. The cross-section structural diagram of novel LSPR biochemical fiber sensor.

The material employed for the metallic layer in this study was gold. The complex refractive index of gold was obtained from the Handbook of Optical Constants of Solids (Academic Press, 1985) [41], and its precise wavelength-dependent fit to the data was obtained using a cubic spline algorithm, as shown in Fig. 1 of Ref. [1]. Surface plasmon resonance (SPR) can generally be divided into two major categories: propagating SPR and localized SPR (LSPR). The observations of the physical SPR properties clearly indicated that collective oscillations occurred at the metal and analyte junctions, which is the critical reason that the SPR and LSPR fiber sensors demonstrate excellent sensitivity when measuring analyte concentration changes. In addition, the LSPR wave did not propagate and its energy was more concentrated on the metal and analyte junctions compared with that of the SPR wave. Therefore, for LSPR fiber sensors, as the number of positions (or particles) where collective electrons oscillation can occur increases, the sensitivity of the senor in measuring analyte concentrations increases. In theory, if the LSPR fiber sensor is properly designed, the sensitivity of the sensor is superior to that of the SPR fiber sensor. In this study, the LSPR design was adopted for developing the sensors. Therefore, any pin on the nano-metal gears can be regarded as a particle. Specifically, the nano-metal cylinder-tessellation array LSPR biochemical fiber sensor contained 24 000 particles (24 000 pins; 80 × 300). In numerous published papers, the size of a cross-section of a particle that can trigger LSPR wave has been typically in the range of 10–60 nm. Based on the structure of the nano-metal cylinder-tessellation array LSPR biochemical fiber sensor proposed in this study, the thickness (d_m) and length (Λ) of nano-metal gears were tested continually. The result showed that when d_m = 20 nm, the minimum length of nano-metal gears that can trigger LSPR wave was 181.1593 nm. Therefore, in this study, unless a specific explanation was provided, the thickness and length of the nanometal ring were 20 nm and 181.1593 nm, respectively [18,19].

LSPR biochemical fiber sensors are extremely sensitive to self-structure parameters, operating wavelengths, and variations in the refractive index of the analyte. Obviously, this high sensitivity will be a disadvantage that cannot be controlled in advance when producing such sensors. Consequently, in the field of LSPR fiber sensors, the responses to the aforementioned parameters have to be understood before practice fabricating [17–19]. This study utilized a powerful numerical technique that combines FEM and EEM to design and simulate this novel LSPR biochemical fiber sensor based on previous studies [1]. Two kinds of high-performance LSPR fiber sensors (i.e., a D-type localized SPR fiber sensor based on nanometal strips [17] and a high-performance localized surface plasmon resonance fiber sensor based on nano-metal-gear array [18]) were successfully designed and researched. From an optical waveguide aspect, a complete eigenmode expansion base must include all modes that can exist in this optical waveguide. Nevertheless, from a numerical calculation aspect, it is impossible to include a complete eigenmode expansion base because of the computation abilities of servers. Moreover, to ensure complete eigenmode expansion bases in simulated environments and increase the precision of the simulation results, the optical fiber structure was transversely enclosed with a PML, and terminated with a PRB, as shown in Figs. 1 and 2. This makes an open and reflectionless environment equivalent to a close and finite computation domain. The primary intention was to discretize the continuum of non-guided radiation modes on the radiation spectra. Subsequently, discrete guided modes, discrete LSPR modes, and discrete radiation modes were integrated to form a complete, orthogonal, and normalizable eigenmode expansion base [42–47]. The equivalence between the open and closed space is detailed in Figs. 3 and 4 of [18]. The PML affects the discrete radiation modes, causing the effective refractive index of the discrete radiation mode to be a complex number $n_n^r = n_n^{r'} + jn_n^{r''}$ and causing the discrete radiation modes to exhibit a dissipation characteristic of $e^{-\alpha_n^r z}$. By gradually increasing the thickness of PML, tests were conducted repeatedly to determine the appropriate thickness. Initially, the PML thickness was set to be small. The energy of the discrete radiation mode was observed to examine whether it could be depleted before being detected. If not, the PML thickness was increased until the detector was not able to detect the energy. Consequently, the PML thickness was determined. In this study, when no explanation was provided, the thickness of PML (d_{PML}) was 0.825 μm [18,19]. The current technology used in semiconductor fabrication is widely recognized, and the nano-metal cylinder-tessellation array LSPR biochemical fiber sensor in this paper can be fabricated using such technology [48–53].

3. The finite element method

The FEM is a full-vectorial numerical method used to solve partial differential equations (PDE) that satisfy boundary conditions, especially with the curved interface. The variational principle, domain cutting, and interpolation function are the core concept of

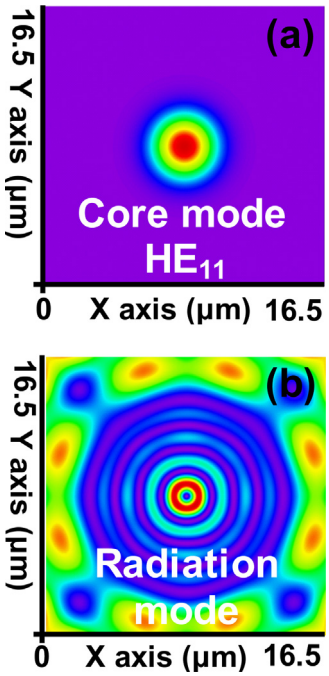

Fig. 3. The 2D power distributions of the core mode HE_{11} and one discrete radiation mode for Segment (a).

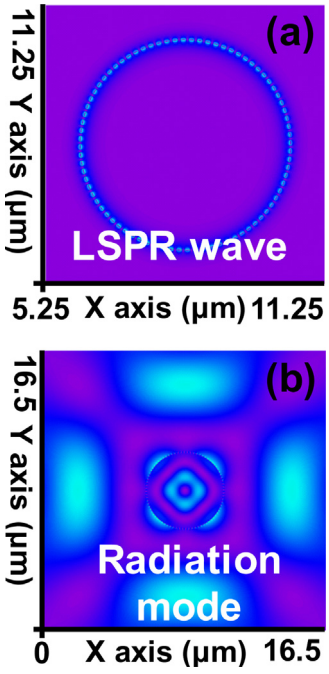

Fig. 4. The 2D power distributions of one discrete LSPR mode and one discrete radiation mode for Segment (b).

this technique. FEM transforms the original problem into functional extreme value problems. Relevant details have been explained in previous studies [1,17–19]. The optical waveguide was transversely enclosed with a PML and terminated with a PRB to improve the numerical calculation accuracy of the nano-metal cylinder-tessellation array LSPR biochemical fiber sensor and reduce the error between the simulation and practical operations by providing more valuable design parameters as a reference for producing actual sensors.

In this paper, the triangular element was used to cut the geometric domain of the *X*–*Y* plane in Segments (a)–(c), as shown in Fig. 2. A high cutting resolution provides more accurate results, although the process involves a substantially higher number of computations. Therefore, appropriate discretization of the target resolved domain is necessary when applying the FEM. As mentioned previously regarding the relationship between the obtained modes and decomposition resolution, theoretically, all modes must be mutually orthogonal. The orthogonality can be represented using Eq. (1) in Ref. [18]. According to the examination mechanism in Ref. [18], whether the orthogonality of the acquired modes for Segments (a)–(c) satisfied the −40 dB criterion was determined.

First, 100 modes consisting of discrete guided modes, discrete LSPR modes, and discrete radiation modes were obtained for the three segments at the operating wavelength of $\lambda = 1550$ nm. Fig. 2 was used to perform resolutions for Segment (a) involving 30 discrete guided and 70 discrete radiation modes. The 2D power distributions of HE_{11} and one discrete radiation mode are shown in Fig. 3. Fig. 4 shows the 2D power distributions of one discrete LSPR mode and one discrete radiation mode for Segment (b). Finally, Fig. 5 shows the 2D power distributions of one discrete LSPR mode and one discrete radiation mode for Segment (c). In a cylindrical coordinate system, if the φ axis is considered a straight, the LSPR fiber sensor exhibits a clear tessellation array.

According to the structural diagram of the metal in Segment (b) of this LSPR biochemical fiber sensor, presented in Fig. 6, and the 2D power distribution of a discrete LSPR wave on the *r* and φ axes of a 20-nm-thick Au layer, as shown in Fig. 4(a), an analogous dipole is excited in the proposed novel LSPR fiber sensor. This finding

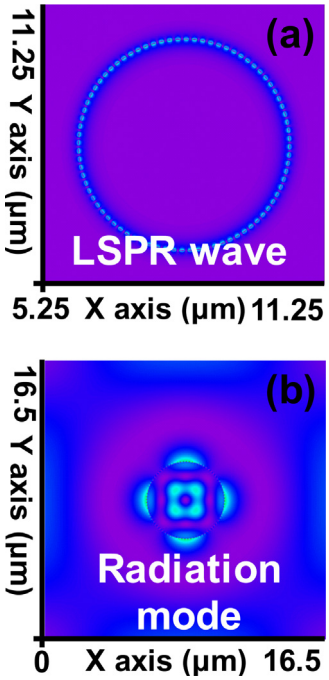

Fig. 5. The 2D power distributions of one discrete LSPR mode and one discrete radiation mode for Segment (c).

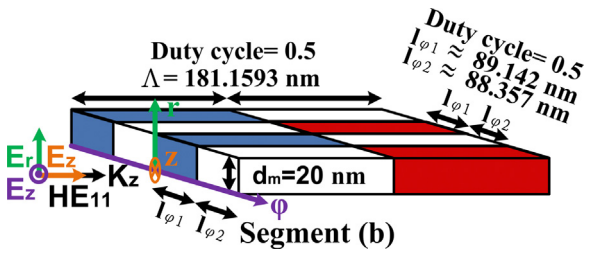

Fig. 6. A structural diagram of the metal (Au) in LSPR fiber sensors for Segment (b).

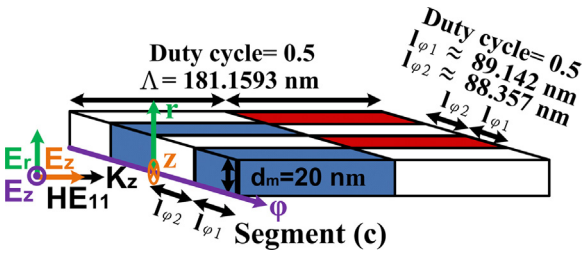

Fig. 7. A structural diagram of the metal (Au) in LSPR fiber sensors for Segment (c).

indicates that the current metallic patterns of fiber sensors can trigger LSPR wave through the electric fields E_r and E_φ of HE_{11}. In addition, according to the structural diagram of metal in Segment (c) of this LSPR biochemical fiber sensor, presented in Fig. 7, and the 2D power distribution of a discrete LSPR wave on the r and φ axes of a 20-nm-thick Au layer, as shown in Fig. 5(a), the current metallic patterns of fiber sensors can trigger LSPR wave through the electric fields E_r and E_φ of HE_{11}. Regarding length (Λ = 181.1593 nm), the LSPR triggered through the electric field E_z of HE_{11} on the z-axis is weaker than that triggered on the r and φ axes. In other words, for this novel LSPR biochemical fiber sensor, the physical phenomenon of LSPR excitation of the optical waveguide in Segments (b) and (c) occurs on the r and φ axes, and dominates the LSPR of the optical waveguide [54,55]. Thus, LSPR generation is the critical reason that this novel fiber sensor yields a high performance.

The three uniform optical waveguides (Segments (a)–(c) in Fig. 1) were separately calculated to assess the orthogonality of all modes obtained using the FEM. The orthogonal values of the 100 obtained modes were calculated and examined; the results are shown in Fig. 8. In addition to each mode possessing a self-orthogonal value of 1 ($10\cdot\log_{10}(1) = 0$ dB), the orthogonal values between two modes satisfied the requirement of being less than 10^{-4} ($10\cdot\log_{10}(10^{-4}) = -40$ dB).

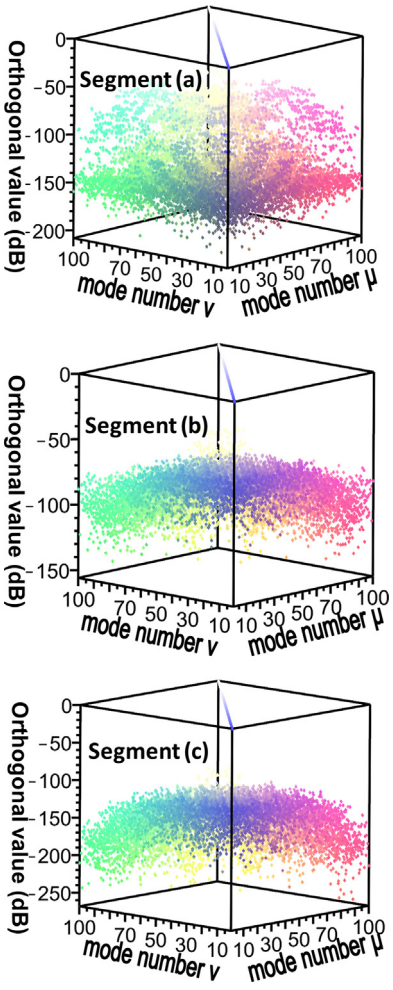

Fig. 8. The relationships between the orthogonal values of the 100 modes in Segments (a)–(c).

4. The eigenmode expansion method

The primary objective of the EEM is to prompt the guided mode to transmit power in the fiber structure. This study proposes a novel LSPR fiber sensor that comprises an SMF, nano-metal rings, and nano-metal gears. Side and cross-sectional diagrams of the sensor structure are presented in Figs. 1 and 2. Each segment object is considered a uniform waveguide that possesses a fixed refractive index value. The contact surface between segment object $k-1$ (Se_{k-1}) and segment object k (Se_k) is called junction $k-1$ (J_{k-1}) as shown in Fig. 9 of Ref. [19]. The modes that may exist in each segment object were recalculated. Next, power conversions between segment objects were performed using the Fourier series expansion method. This method can also be employed to complete power transfers for the entire LSPR fiber sensor [1,17–19].

This indicates that the guided modes existing in the same segment of a periodic component are identical. Therefore, when using the FEM to solve guided modes, only one segment must be calculated. This considerably reduces the computation time and memory required for the entire component simulation. In summation, combining the FEM with the EEM is particularly suitable for designing periodic components.

After the propagated electromagnetic fields for a uniform segment object Se_{k-1} are obtained, power must be precisely transferred from segment object Se_{k-1} to segment object Se_k. Based on Fourier series expansion concept and the orthogonality of the modes, the coefficients for each forward ($C_m^{f,k}$) and backward ($C_m^{b,k}$) mode field in the uniform waveguide (segment k) can be expressed as the following [19]:

$$C_m^{f,k} = \sum_{\ell=1}^{L} C_n^{f,k-1} e^{i(\beta_\ell^{k-1}-\beta_m^k)z} \left[\frac{\langle \vec{e}_{t\ell}^{\,k-1}, \vec{h}_{tm}^{\,k} \rangle + \langle \vec{e}_{tm}^{\,k}, \vec{h}_{t\ell}^{\,k-1} \rangle}{\langle \vec{e}_{tm}^{\,k}, \vec{h}_{tm}^{\,k} \rangle} \right] + \sum_{\ell=1}^{L} C_n^{b,k-1} e^{-i(\beta_\ell^{k-1}+\beta_m^k)z} \left[\frac{\langle \vec{e}_{t\ell}^{\,k-1}, \vec{h}_{tm}^{\,k} \rangle - \langle \vec{e}_{tm}^{\,k}, \vec{h}_{t\ell}^{\,k-1} \rangle}{\langle \vec{e}_{tm}^{\,k}, \vec{h}_{tm}^{\,k} \rangle} \right] \quad (1)$$

$$C_m^{b,k} = \sum_{\ell=1}^{L} C_n^{f,k-1} e^{i(\beta_\ell^{k-1}+\beta_m^k)z} \left[\frac{\langle \vec{e}_{t\ell}^{\,k-1}, \vec{h}_{tm}^{\,k} \rangle - \langle \vec{e}_{tm}^{\,k}, \vec{h}_{t\ell}^{\,k-1} \rangle}{\langle \vec{e}_{tm}^{\,k}, \vec{h}_{tm}^{\,k} \rangle} \right] + \sum_{\ell=1}^{L} C_n^{b,k-1} e^{-i(\beta_\ell^{k-1}-\beta_m^k)z} \left[\frac{\langle \vec{e}_{t\ell}^{\,k-1}, \vec{h}_{tm}^{\,k} \rangle + \langle \vec{e}_{tm}^{\,k}, \vec{h}_{t\ell}^{\,k-1} \rangle}{\langle \vec{e}_{tm}^{\,k}, \vec{h}_{tm}^{\,k} \rangle} \right], \quad (2)$$

where $M = L = 100$ was the mode amount. Finally, the propagation effect of the proposed LSPR fiber sensor was accurately completed and simulated using the Fourier series expansion method. After considering the detailed description of the EEM, this study determined that only one segment object was required for periodic objects. In other words, by calculating only one segment object, this study completed the simulation of the period object's power transfer phenomenon.

According to the detailed description of the EEM, M and L represent the number of guided modes and can critically affect the

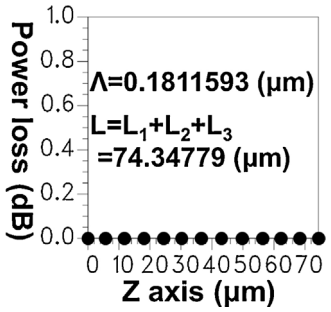

Fig. 9. The relationship between the eigenmode mode expansion position and power loss when employing the 100 modes.

accuracy of the results. From a mathematical perspective, Fourier series expansion must include all guided modes that existed in the structure. However, this is impossible for numerical simulations because the time and memory required to perform such calculations are excessive and unfeasible.

However, if the number of modes is insufficient, power loss will occur during each pass through the scattering matrix of the adjacent segment object junction. From a numerical standpoint, it is impossible to use all the modes for computation, which is to say that dissipations are inevitable, but we must bring it to the minimum. That is why we have also set an acceptable upper threshold for EEM, which is at 10^{-4} ($10\cdot\log_{10}(10^{-4}) = -40$ dB). During simulations, we first tried using different numbers of modes (eigenvectors), and the power dissipation was calculated. The result was then checked to see if it was smaller than 10^{-4} ($10\cdot\log_{10}(10^{-4}) = -40$ dB). If this upper threshold was not satisfied, the number of modes (eigenvectors) was increased. This method was used until the number of modes (eigenvectors) that satisfy the dissipation threshold was found. Therefore, this study adopted the reverse thinking method and searched for the minimum M (or L) value that satisfied the requirement of a power loss value below 10^{-4} ($10\cdot\log_{10}(10^{-4}) = -40$ dB). Fig. 9 shows the calculation results of the mode expansion positions and power losses when the 100 modes were employed; the results evidently satisfied aforementioned requirement [17–19].

5. Design and simulation

Summarizing the numerical simulation methods described in Sections 3 and 4, this section proposes a rigorous, simplistic, and comprehensive process for analyzing and designing this novel LSPR biochemical fiber sensor. This procedure involves performing the following five procedures: (a) solve all guided modes using the FEM; (b) use the EEM to perform an algorithm for power transmission; (c) test whether the power loss obtained using the EEM satisfies the less than 10^{-4} ($10\cdot\log_{10}(10^{-4}) = -40$ dB) requirement; (d) calculate the resolution of the LSPR fiber sensor; and (e) calculate the sensitivity of the sensor.

After this LSPR biochemical fiber sensor was designed according to the aforementioned parameters, the core mode (as shown in Fig. 3(a)) was input into the left end of the sensor, as shown in Fig. 1. The power transmission (Poynting vector P_Z) algorithm was then performed using the EEM; the results are shown in Fig. 10(a). To further observe the newly structured LSPR sensor, the view A region in Fig. 10(a) was magnified and presented in Fig. 10(b), which clearly shows LSPR excitation.

Resolution and sensitivity are two crucial indicators for evaluating the quality of all sensors. In this study, these indicators were evaluated using the calculation results of the LSPR biochemical fiber sensor spectrum. For obtaining actual spectrum measurements of LSPR biochemical sensor, optical spectra analyzers (OSAs) are the

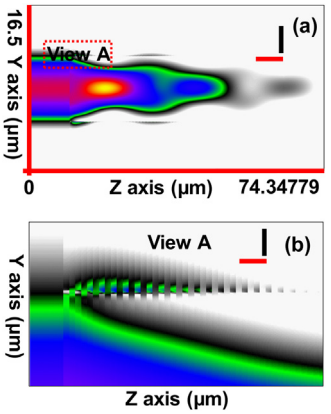

Fig. 10. (a) The Y–Z plane power transmission (Poynting vector P_Z) of the core mode, and (b) a magnified image of the View A region in (a) with scale bar 13 and 55 μm for z-axis and scale bar 22 and 125 μm for y-axis.

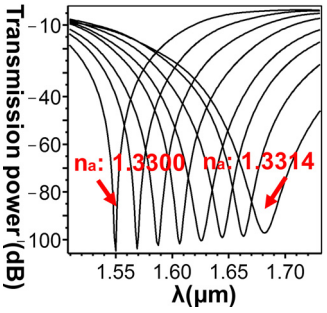

Fig. 11. Spectrum changes for the LSPR fiber sensor when the analyte refractive index n_a changed.

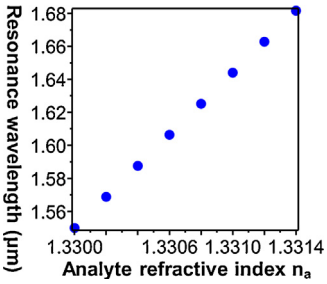

Fig. 12. The relationships between the analyte refractive index n_a and the LSPR's resonance wavelength.

instrument most commonly employed. However, this raises concerns regarding how sensors can differentiate LSPR dips from noise. The resolution of LSPR sensors influences the ability to distinguish LSPR dips from noise using an OSA.

In spectra diagrams, shifts in the resonance wavelength reflect the LSPR sensor sensitivity to changes in the refractive index of an analyte. To analyze the spectral characteristics of the proposed LSPR biochemical fiber sensor, the bar transmission power was calculated based on Eq. (8) in Ref. [18]. Calculations of the core mode spectral patterns for various analytes are shown in Fig. 11. Specifically, the analyte refractive index changed from $n_a = 1.3300$ to $n_a = 1.3314$. Fig. 11 shows that the proposed LSPR biochemical sensor possesses a high resolution of approximately −110 dB. Fig. 12 is a diagram that illustrates the relationship between the resonance wavelength and analyte refractive index shown in Fig. 11. According to Fig. 12, the resonance wavelength of the LSPR biochemical sensor shifted from 1.55 to 1.681582 μm when the analyte refractive index changed from $n_a = 1.3300$ to $n_a = 1.3314$.

Consequently, the sensor sensitivity can be calculated as follows [1,17–19]:

$$Sensitivity \approx \frac{(1.681582 - 1.550000)}{(1.3314 - 1.3300)} \approx 93987\ \text{nm/RIU} \quad (3)$$

where RIU represents the refractive index unit. The results indicate that the proposed LSPR biochemical fiber sensor possesses high sensitivity of approximately 93 987 nm/RIU.

From the optic characteristics of the LSPR indicated that electrons collectively oscillated on the junctions between metal and analytes. It was the critical factor causing the LSPR fiber sensors to be highly sensitive to analyte concentration variations. Therefore, for the LSPR fiber sensor, as the number of positions (or particles) where collective electrons oscillation can occur increases, the sensitivity of this sensor in measuring analyte concentrations increases. When the nano-metal cylinder-tessellation array LSPR biochemical fiber sensor, the novel D-shape LSPR fiber sensor [17], and the high-performance localized surface plasmon resonance fiber sensor based on nano-metal-gear array [18] were compared, the structural parameters of these sensors clearly indicated that the nano-metal cylinder-tessellation array LSPR fiber sensor contained far more particles compared with those of the other two sensors. Specifically, the nano-metal cylinder-tessellation array LSPR fiber sensor contained 24 000 particles (24 000 pins; 80×300). By contrast, the novel D-shape LSPR fiber sensor contained 1614 particles [17], and the high-performance localized surface plasmon resonance fiber sensor based on nano-metal-gear array contained 4100 particles [18].

According to the previous descriptions regarding the LSPR physical characteristics, as the number of particles increases, a larger number of collective electrons oscillation positions are exhibited, and thus the ability of the sensor to measure analyte concentration changes increases. The D-shaped LSPR fiber sensor developed in [17] exhibited an approximate length of 2494.4301 μm, a resolution of approximately −35 dB, and a sensitivity of approximately 20 183.333 nm/RIU. The high-performance localized surface plasmon resonance fiber sensor based on nano-metal-gear array developed in [18] exhibited an approximate length of 77.01764 μm, a resolution of approximately −80 dB, and a sensitivity of approximately 45 062 nm/RIU. The LSPR fiber sensor designed in this study possesses the advantageous attributes of a short length (74.34779 μm), high resolution (approximately −110 dB), and high sensitivity (approximately 93 987 nm/RIU). As far as I know, up to present it possesses the best resolution and sensitivity compared with the other LSPR sensors.

6. Conclusion

A novel LSPR fiber sensor comprising an SMF and two types of nano-metal gears was developed in this study. A numerical simulation method that integrates the FEM and EEM was employed to design and analyze the proposed LSPR fiber sensor. To increase the accuracy of the simulation results, the waveguide structure was transversely enclosed with a PML, and terminated with a PRB. This generates an open and reflectionless environment equivalent to the original physical domain yet located in a close and finite computation domain. The primary purpose was to discretize the continuum of non-guided radiation modes and integrate discrete guided modes, discrete LSPR modes, and discrete radiation modes to establish a complete, orthogonal, and normalizable eigenmode expansion base. Using the improved eigenmode expansion base, the simulation results of the proposed LSPR fiber sensor can provide valuable data as a reference for producing practical modes, and thereby reduce the gap between simulations and practical operations. According to a structural diagram of the metal (Au) in Segments (b) and (c) of the proposed LSPR fiber sensor, the 2D power distribution of the LSPR wave on the r and φ axes of a 20-nm-thick Au layer was solved using the FEM. The results show that an analogous dipole was excited in the proposed LSPR fiber sensor. This finding indicates that the current metallic patterns of fiber sensors can trigger LSPR through the electric fields E_r and E_φ of the core mode HE_{11}. In the novel LSPR fiber sensor, the physical phenomenon of LSPR excitation of the waveguides in Segments (b) and (c) occurs on the r and φ axes, and dominates the LSPR of the waveguides. LSPR generation is the primary reason that the novel fiber sensor yields a high performance. The simulation results facilitated in-depth observations of LSPR. Subsequently, an LSPR fiber sensor with the characteristics of a short length (74.34779 μm), high resolution (approximately −110 dB), and high sensitivity (approximately 93 987 nm/RIU) was fabricated. As far as I know, up to present it possesses the best resolution and sensitivity compared with the other LSPR sensors.

Acknowledgment

The author gratefully acknowledges the support provided for this study by the Ministry of Science and Technology (MOST 103-2221-E-167-001) of Taiwan.

References

[1] Y.J. He, Investigation of LPG–SPR sensors using the finite element method and eigenmode expansion method, Opt. Express 21 (2013) 13875–13895.
[2] J. Cao, E.K. Galbraith, T. Sun, K.T.V. Grattan, Cross-comparison of surface plasmon resonance-based optical fiber sensors with different coating structures, IEEE Sens. J. 12 (2012) 2355–2361.
[3] P. Bhatia, B.D. Gupta, Surface-plasmon-resonance-based fiber-optic refractive index sensor: sensitivity enhancement, Appl. Opt. 50 (2011) 2032–2036.
[4] M. Gu, P. Bai, E.P. Li, Enhancing the reception of propagating surface plasmons using a nanoantenna, IEEE Photon. Technol. Lett. 22 (2010) 245–247.
[5] X. Yu, S. Zhang, Y. Zhang, H.P. Ho, P. Shum, H. Liu, D. Liu, An efficient approach for investigating surface plasmon resonance in asymmetric optical fibers based on birefringence analysis, Opt. Express 18 (2010) 17950–17957.
[6] K.H. An, M. Shtein, K.P. Pipe, Surface plasmon mediated energy transfer of electrically pumped excitons, Opt. Express 18 (2010) 4041–4048.
[7] L.Y. Shao, Y. Shevchenko, J. Albert, Intrinsic temperature sensitivity of tilted fiber Bragg grating based surface plasmon resonance sensors, Opt. Express 18 (2010) 11464–11471.
[8] A. Wang, A. Docherty, B.T. Kuhlmey, F.M. Cox, M.C.J. Large, Side-hole fiber sensor based on surface plasmon resonance, Opt. Lett. 34 (2009) 3890–3892.
[9] Y.C. Lu, W.P. Huang, S.S. Jian, Influence of mode loss on the feasibility of grating-assisted optical fiber surface plasmon resonance refractive index sensor, J. Lightwave Technol. 27 (2009) 4804–4808.
[10] D. Choi, I.M. Lee, J. Jung, J. Park, J.H. Han, B. Lee, Metallic-grating-based interconnector between surface plasmon plariton waveguides, J. Lightwave Technol. 27 (2009) 5675–5680.
[11] B. Špačková, J. Homola, Theoretical analysis of a fiber optic surface plasmon resonance sensor utilizing a Bragg grating, Opt. Express 17 (2009) 23254–23264.
[12] Y.S. Jung, J. Wuenschell, H.K. Kim, P. Kaur, D.H. Waldeck, Blue-shift of surface plasmon resonance in a metal nanoslit array structure, Opt. Express 17 (2009) 16081–16091.
[13] J. Wang, X. Chen, W. Lu, High-efficiency surface plasmon polariton source, J. Opt. Soc. Am. B 26 (2009) B139–B142.
[14] G. Nemova, R. Kashyap, Modeling of plasmon-polariton refractive-index hollow core fiber sensors assisted by a fiber Bragg grating, J. Lightwave Technol. 24 (2006) 3789–3796.
[15] Y.J. He, Y.L. Lo, J.F. Huang, Optical-fiber surface-plasmon-resonance sensor employing long-period fiber gratings in multiplexing, J. Opt. Soc. Am. B 23 (2006) 801–811.
[16] Ó. Esteban, R. Alonso, M.C. Navarrete, A. González-Cano, Surface plasmon excitation in fiber-optics sensors: a novel theoretical approach, J. Lightwave Technol. 20 (2002) 448–453.
[17] Y.J. He, Novel D-shape LSPR fiber sensor based on nano-metal strips, Opt. Express 21 (2013) 23498–23510.
[18] Y.J. He, High-performance localized surface plasmon resonance fiber sensor based on nano-metal-gear array, Sens. Actuators B 193 (2014) 778–787.
[19] Y.J. He, Nanometal ring-array LSPR fiber sensor based on the perfectly matched layer and perfectly reflecting boundary, Sens. Actuators B (2014), http://dx.doi.org/10.1016/j.snb.2014.05.093 (in press).
[20] H.Y. Lin, C.H. Huang, G.L. Cheng, N.K. Chen, H.C. Chui, Tapered optical fiber sensor based on localized surface plasmon resonance, Opt. Express 20 (2012) 21693–21701.

[21] R. Dutta, R. Bharadwaj, S. Mukherji, T. Kundu, Study of localized surface-plasmon-resonance-based optical fiber sensor, Appl. Opt. 50 (2011) E138–E144.
[22] Y. Liu, Y. Zou, R.G. Lindquist, A reflection-based localized surface plasmon resonance fiber-optic probe for biochemical sensing, Biomed. Opt. Express 2 (2011) 478–484.
[23] C.Y. Tsai, S.P. Lu, J.W. Lin, P.T. Lee, High sensitivity plasmonic index sensor using slablike gold nanoring arrays, Appl. Phys. Lett. 98 (2011) 153108.
[24] S.K. Srivastava, B.D. Gupta, Simulation of a localized surface-plasmon-resonance-based fiber optic temperature sensor, J. Opt. Soc. Am. A 27 (2010) 1743–1749.
[25] R. Marty, G. Baffou, A. Arbouet, C. Girard, R. Quidant, Charge distribution induced inside complex plasmonic nanoparticles, Opt. Express 18 (2010) 3035–3044.
[26] M.J. Kofke, D.H. Waldeck, G.C. Walker, Composite nanoparticle nanoslit arrays: a novel platform for LSPR mediated subwavelength optical transmission, Opt. Express 18 (2010) 7705–7713.
[27] W.Y. Ma, H. Yang, J.P. Hilton, Q. Lin, J.Y. Liu, L.X. Huang, J. Yao, A numerical investigation of the effect of vertex geometry on localized surface plasmon resonance of nanostructure, Opt. Express 18 (2010) 843–853.
[28] H.Y. Lin, C.H. Huang, C.H. Chang, Y. Chiang Lan, H.C. Chui, Direct near-field optical imaging of plasmonic resonances in metal nanoparticle pairs, Opt. Express 18 (2010) 165–172.
[29] V.V.R. Sai, T. Kundu, S. Mukherji, Novel U-bent fiber optic probe for localized surface plasmon resonance based biosensor, Biosens. Bioelectron. 24 (2009) 2804–2809.
[30] M.Y. Ng, W.C. Liu, Fluorescence enhancements of fiber-optic biosensor with metallic nanoparticles, Opt. Express 17 (2009) 5867–5878.
[31] S.K. Srivastava, R.K. Verma, B.D. Gupta, Theoretical modeling of a localized surface plasmon resonance based intensity modulated fiber optic refractive index sensor, Appl. Opt. 48 (2009) 3796–3802.
[32] S.J. Yoon, D. Kim, Target dependence of the sensitivity in periodic nanowire-based localized surface plasmon resonance biosensors, J. Opt. Soc. Am. A 25 (2008) 725–735.
[33] D.F.G. Gallagher, T.P. Felici, Eigenmode expansion methods for simulation of optical propagation in photonics – pros and cons, Proc. SPIE 4987 (2003) 69–82.
[34] J.J. Wu, H.E. Lin, T.J. Yang, Y.H. Kao, H.L. Chiueh, D.J. Hou, Open waveguide based on low frequency spoof surface plasmon polaritons, J. Electromagnet. Anal. Appl. 5 (2013) 58–62.
[35] A. Rusina, M. Durach, M.I. Stockman, Theory of spoof plasmons in real metals, Appl. Phys. A 100 (2010) 375–378.
[36] M. Navarro-Cía, M. Beruete, S. Agrafiotis, Broadband spoof plasmons and subwavelength electromagnetic energy confinement on ultrathin metafilms, Opt. Express 17 (2009) 18184–18195.
[37] Q. Gan, Z. Fu, Y.J. Ding, F.J. Bartoli, Ultra-wide band slow light system based on THz plasmonic graded metal grating structures, Phys. Rev. Lett. 100 (2008) 256803.
[38] C.R. Williams, S.R. Andrews, S.A. Maier, A.I. Fernández-Domínguez, L. Martín-Moreno, F.J. García-Vidal, Highly confined guiding of terahertz surface plasmon polaritons on structured metal surfaces, Nat. Photon. 2 (2008) 175–179.
[39] A.I. Fernández-Domínguez, L. Martín-Moreno, F.J. García-Vidal, S.R. Andrews, S.A. Maier, Spoof surface plasmon polariton modes propagating along periodically corrugated wires, IEEE J. Sel. Top. Quantum Electron. 16 (2008) 1515–1521.
[40] S.A. Maier, S.R. Andrews, L. Martín-Moreno, F.J. García-Vidal, Terahertz surface plasmon polariton propagation and focusing on periodically corrugated metal wires, Phys. Rev. Lett. 97 (2006) 176805.
[41] E.D. Palik, Handbook of Optical Constants of Solids, Academic Press, Orlando, FL, 1985.
[42] W.P. Huang, J. Mu, Complex coupled-mode theory for optical waveguides, Opt. Express 17 (2009) 19134–19152.
[43] J. Mu, W.P. Huang, Simulation of three-dimensional waveguide discontinuities by a full-vector mode-matching method based on finite-difference schemes, Opt. Express 16 (2008) 18152–18163.
[44] K. Jiang, W.P. Huang, Finite-difference-based mode-matching method for 3-D waveguide structures under semivectorial approximation, J. Lightwave Technol. 23 (2005) 4239–4248.
[45] H. Derudder, F. Olyslager, D. De Zutter, S. Van den Berg he, Efficient mode-matching analysis of discontinuities in finite planar outer claddings using perfectly matched layers, IEEE Trans. Antennas Propag. 49 (2001) 185–195.
[46] W.P. Huang, C.L. Xu, W. Lui, K. Yokoyama, The perfectly matched layer (PML) boundary conditions for modal analysis of optical waveguides: leaky mode calculations, IEEE Photon. Technol. Lett. 8 (1996) 652–654.
[47] W.C. Chew, J.M. Jin, E. Michielssen, Complex coordinate stretching as a generalized absorbing boundary condition, Microw. Opt. Technol. Lett. 15 (1997) 363–369.
[48] W.C. Chuang, A.C. Lee, C.K. Chao, C.T. Ho, Fabrication of optical filters based on polymer asymmetric Bragg couplers, Opt. Express 17 (2009) 18003–18013.
[49] W.S. Weng, W.C. Chuang, I.F. Shyu, A.C. Lee, C.T. Ho, The fabrication of the Bragg grating on the D-shaped fiber, in: IEEE Opto-Electronics and Communications Conference, 2009.
[50] V.P. Drachev, U.K. Chettiar, A.V. Kildishev, H.K. Yuan, W. Cai, V.M. Shalaev, The Ag dielectric function in plasmonic metamaterials, Opt. Express 16 (2008) 1186–1195.
[51] Y.C. Lin, W.H. Tsai, Y.C. Tsao, J.K. Tai, An enhanced optical multimode fiber sensor based on surface plasmon resonance with cascaded structure, IEEE Photon. Technol. Lett. 20 (2008) 1287–1289.
[52] K.M. Byun, S.J. Yoon, D. Kim, S.J. Kim, Experimental study of sensitivity enhancement in surface plasmon resonance biosensors by use of periodic metallic nanowires, Opt. Lett. 32 (2007) 1902–1904.
[53] K. Cottier, M. Wiki, G. Voirin, H. Gao, R.E. Kunz, Label-free highly sensitive detection of (small) molecules by wavelength interrogation of integrated optical chips, Sens. Actuators B 91 (2003) 241–251.
[54] M. Hu, J.Y. Chen, Z.Y. Li, L. Au, G.V. Hartland, X.D. Li, M. Marquez, Y.N. Xia, Gold nanostructures: engineering their plasmonic properties for biomedical applications, Chem. Soc. Rev. 35 (2006) 1084–1094.
[55] J. Renger, Excitation, interaction, and scattering of localized and propagating surface polaritons (Ph.D. Thesis), Technical University, Dresden, 2006.

Biography

Yue Jing He received his M.S. degree from the Department of Communication Engineering at National Chiao-Tung University, Hsinchu, Taiwan, in 2000, and his Ph.D. degree from the Department of Electrical Engineering at National Cheng Kung University, Tainan, Taiwan, in 2006. After graduation, he has been a member of the faculty of the Electronic Engineering Department, National Chin-Yi University of Technology, Taichung, Taiwan, since 2008. His research interests are in the areas of the component design in optical fiber communication and in surface plasmon resonance sensor.